Enhanced cadmium removal by biochar and iron oxides composite : Material interactions and pore structure

Journal of Environmental Management

Liu, Yong; Wang, Long; Liu, Chang; Ma, Jie; Ouyang, Xiaoxue et al

https://doi.org/10.1016/j.jenvman.2022.117136

Journal of Environmental Management 330 (2023) 117136

Contents lists available at ScienceDirect

Journal of Environmental Management

journal homepage: www.elsevier.com/locate/jenvman

Research article

Enhanced cadmium removal by biochar and iron oxides composite: Material interactions and pore structure

Yong Liu [a,b,1], Long Wang [a,b,c,1], Chang Liu [a,b], Jie Ma [a,b,*], Xiaoxue Ouyang [a,b], Liping Weng [a,b,d], Yali Chen [a,b], Yongtao Li [e,f]

[a] Key Laboratory for Environmental Factors Control of Agro-Product Quality Safety, Ministry of Agriculture and Rural Affairs, Tianjin, 300191, China
[b] Agro-Environmental Protection Institute, Ministry of Agriculture and Rural Affairs, Tianjin 300191, China
[c] College of Resources and Environment, Henan Agricultural University, Zhengzhou 450002, China
[d] Department of Soil Quality, Wageningen University, Wageningen, the Netherlands
[e] College of Resource and Environmental Engineering, Jiangxi University of Science and Technology, Ganzhou Jiangxi, 341000, China
[f] College of Natural Resources and Environment, South China Agricultural University, Guangzhou, 510642, China

ARTICLE INFO

Keywords:
Cadmium
Straw biochar
Ferrihydrite
Goethite
Quantum chemical calculation

ABSTRACT

The combination of biochar (BC) and iron minerals improves their pollutant adsorption capacity. However, little is known about the reactivity of BC-iron mineral composites regarding their interaction and change in the pore structure. In this study, the mechanism of cadmium (Cd) adsorption by BC-iron oxide composites, such as BC combined with ferrihydrite (FH) or goethite (GT), was explored. The synergistic effect of the BC-FH composite significantly improved its Cd adsorption capacity. The adsorption efficiencies of BC-FH and BC-GT increased by 15.0% and 10.8%, respectively, compared with that of uncombined BC, FH, and GT. The strong Cd adsorption by BC-FH was attributed to stable interactions and stereoscopic pore filling between BC and FH. The scanning electron microscopy results showed that FH particles entered the BC pores, whereas GT particles were loaded onto the BC surface. FTIR spectroscopy showed that GT covered a larger area of the BC surface than FH. After loading FH and GT, BC porosities decreased by 9.3% and 4.1%, respectively. Quantum chemical calculations and independent gradient mode analysis showed that van der Waals interactions, H-bonds, and covalent-like interactions maintained stability between iron minerals and BC. Additionally, humic acid increased the agglomeration of iron oxides and formed larger particles, causing additional aggregates to load onto the BC surface instead of entering the BC pores. Our results provide theoretical support to reveal the interfacial behavior of BC-iron mineral composites in soil and provide a reference for field applications of these materials for pollution control and environmental remediation.

1. Introduction

Farmland and water pollution by toxic heavy metals has become a global concern with the fast-developing manufacturing industry. Heavy metals such as cadmium (Cd) have become environmental hazards owing to their high toxicity, non-biodegradability, and widespread existence in natural and man-made environments (Dai et al., 2021). Cd is widely used as a raw material in metal smelting, which aggravates Cd pollution in the soil (Wang et al., 2021). In China, more than 13,000 ha of land is currently contaminated with Cd, which has been listed as the most urgent heavy metal pollutant (Fu et al., 2021). Exposure to Cd, even at trace levels, can cause serious health issues in humans (Liang et al., 2019), such as cancer, chronic cardiovascular issues, nervous system diseases, and kidney diseases (Wang et al., 2021). Therefore, it is necessary to apply an efficient and reliable technique to remove Cd from soil and soil pore water.

Thus far, various technologies and processes, including adsorption (Maatar and Boufi, 2015), flocculation (Navarro et al., 2003), sedimentation (Machado et al., 2008), and biological remediation (Suresh Kumar et al., 2015) have been applied to remove heavy metal ions.

* Corresponding author.. Key Laboratory for Environmental Factors Control of Agro-Product Quality Safety, Ministry of Agriculture and Rural Affairs, Tianjin, 300191, China. (Jie Ma).
E-mail address: majie@caas.cn (J. Ma).
[1] Yong Liu and Long Wang contributed equally to this study and should be regarded as first joint authors.

https://doi.org/10.1016/j.jenvman.2022.117136
Received 31 October 2022; Received in revised form 6 December 2022; Accepted 21 December 2022
Available online 28 December 2022

Among different methods, adsorption has been accepted as one of the most advantageous techniques owing to its high removal efficiency, simple operation, and low cost (Ali et al., 2018).

Currently, biochar (BC) adsorption is recognized as an efficient and economical method to eliminate Cd pollution (Ahmad et al., 2018). The material produced by the pyrolysis of carbon-containing waste biomass under oxygen-deficient conditions (O'Laughlin and McElligott, 2009). The removal of Cd by BC has been previously reported (Yin et al., 2022). Switchgrass BC produced via hydrothermal carbonization was effectively used in Cd removal (Regmi et al., 2012). Activated Ipomoea BC can effectively remove Cd from water because of its large specific surface area and pore volume (Goswami et al., 2016). To sum up, the mechanism of Cd adsorption by BC can be summed as follows: (i) precipitation by carbonates (CO_3^{2-}) and phosphates (PO_4^{3-}); (ii) complex formation by surface functional groups, for instance, OH^+ and COO^-; (iii) exchange by surface exchangeable cations (K, Ca, and Na); and (iv) coordination by C═C functional groups (Ahmad et al., 2014; Cui et al., 2016; Park et al., 2019). However, owing to its own structural defects, the adsorption capacity of pristine BC is still limited (Jung et al., 2018), and further modification is needed.

The modification of BC with iron oxide significantly improved its heavy metal removal ability (Zhu et al., 2020). Iron mineral is a widely distributed natural nanoparticle found in sediments and soil (Ma et al., 2019). Ferrihydrite (FH) and goethite (GT) are the most common forms of iron oxide found in nature and are known to strongly influence the adsorption and co-precipitation of contaminants such as Cd in the natural environment (Jing et al., 2021; Ma et al., 2018), especially in the nano-state. For example, Fe-based nanoparticles could decrease around 80% Cd accumulation in wheat grains (Hussain et al., 2021). Li et al. (2022) found that soluble Cd in soil was adsorbed or precipitated by Fe compounds. In addition, heavy metals are bound more firmly to GT than to soil (Venema et al., 1996). Randall et al. (1999) pointed out that the mechanism of Cd bonding with iron oxide mineral was inner sphere bonding, and Cd mainly adsorbs to GT at corner sharing sites on the (110) crystal plane by the formation of a bidentate complex.

Therefore, iron oxide modified BC attracted substantial attention and was employed for Cd removal with the advantages of cost effectiveness, facile availability, and environmental benignancy. The loading of iron minerals onto the BC surface can improve the specific surface area and adsorption sites in BC (Yang et al., 2020). For instance, Liu et al. (2020) found that the capacity for Cd adsorption by BC-iron mineral composites was significantly higher than that by BC only. Similarly, the BC-FH composites significantly reduced Cd concentrations in soil pore and leachate water (Ouyang et al., 2021). Moreover, the coupling effect of porous BC with nano-iron oxide enhanced the Cd adsorption, and greatly reduced Cd toxicity (Zhu et al., 2019). The covalent or non-covalent interactions bonding BC and iron minerals may be vital in improving Cd adsorption. However, little is known about the Cd adsorption onto BC-iron mineral composites based on the interactions between BC and iron minerals. Hence, it is urgent to determine the mechanism of the interaction between biochar and iron oxide.

Coupling between the surface properties of BC and iron oxides is assumed to occur based on the findings from research that imply coupling mechanisms would drastically improve the remediation efficiency. Environmental conditions, such as pH and dissolved organic matter (DOM), affect the surface charge of both BC and iron oxides, thereby affecting the environmental behavior of heavy metals. Generally, pH can facilitate or hinder electrostatic interactions by affecting the surface charge density or concentration of metal ions in aqueous solutions by affecting metal deposition reactions and ion exchange (Jefferson et al., 2015). In addition to pH, the impact of DOM is another important factor. Our previous research found that BC can also provide DOM with a very high humification index (Ma et al., 2022; Qian et al., 2020). Humus on the surface of iron minerals can improve their adsorption by changing the ionic charge state, surface roughness, specific surface area, and other physical and chemical properties of the mineral surface (Amini et al., 2020). Humic acid (HA) is the main component of humus (Liu et al., 2021). When HA adsorbs Cd, it promotes iron minerals to block further movement of Cd through coagulation. However, the effects of DOM on Cd adsorption by BC and iron oxides are poorly understood.

In this study, we employed BC as the absorbent material and loaded two different particle diameters of iron oxide (FH and GT) to evaluate: (1) the Cd adsorption properties of BC, iron oxides, and their complexes; and (2) the effect of material interaction and changes in pore structure on Cd immobilization, especially in the presence of HA.

2. Materials and methods

2.1. Preparation and characterization of materials

Commercially available wheat straw-based biochar was used for the treatment experiments. Solid BC was ground and sieved through 100 mesh (0.15 mm), and used as the finished product. FH and GT were synthesized according to the procedures described in a previous study (Schwertmann and Cornell, 2008). Humic acid was extracted using the alkali/acid fractionation mode (Valdrighi et al., 1996). The humus (Macklin Biochemical Co., Ltd.) was dissolved in NaOH (pH = 13) by shaking the mixture at 25 °C for 24 h. After allowing to settle for 12 h, the mixture was centrifuged for 10 min at 2000 rpm to separate the solution and the suspended solids. The supernatant was then decanted slowly, and HA was obtained by titrating the supernatant with HCl to pH 3.0. The HA precipitates were then shaken thrice for 6 h with 0.1 M HCl and washed with Milli-Q ultrapure water until the electrical conductivity (EC) was <10 μS. The pH (solid-solvent ratio was 1:5) values of BC, FH, and GT was measured at 0.05 M $CaCl_2$. The specific surface areas of BC, GT, and FH as measured by Brunauer-Emmett-Teller N_2 (ASAP2460, Micromeritics) adsorption isotherms.

2.2. Batch adsorption experiments

Samples (0.1 mg each) of BC, iron oxides (FH and GT), or a homogeneous mixture of the BC and iron oxides (in a ratio of 1:1 (w/w)) was added into gas-tight 50 mL polyethylene centrifuge tubes, to which the appropriate amount of stock solutions of electrolyte background and adsorbate ions were added in N_2 atmosphere. The volume of the suspension in each tube was 25 mL. The Cd concentrations (added from $CdCl_2$ stock solutions) were 2–200 mg L^{-1} for isothermal adsorption experiments, and the final electrolyte background concentration was 0.01 M NaCl. After adsorption, the binding form of Cd on solid substances was extracted by sequential extraction method. The specific details of the batch adsorption experiments and the modified sequential extraction procedure can be found in the SI S2.

2.3. Quantum chemical calculation

Optimized molecular structures of BC (Tian et al., 2020) and crystal structures of FH (Chappell et al., 2017) and GT (Russell et al., 2009) were constructed to investigate the interactions between BC and iron minerals. The molecular formulas are shown in a previous study (Liu et al., 2022). The complex configuration was performed using Molclus program (Lu, 2021). More than two hundred initial configurations were built, and each configuration was optimized based on PM 6 using Gaussian 16 (Frisch et al., 2016). The single-point energy of selected configuration was then calculated at the B3LYP/6-31G(d) level, in which the element was adopted as the Lanl2DZ basis set. Grimme's D3BJ dispersion was used to describe the intermolecular interactions in all the calculations. Independent gradient mode (IGM) analysis was performed with Multiwfn (Lu and Chen, 2012).

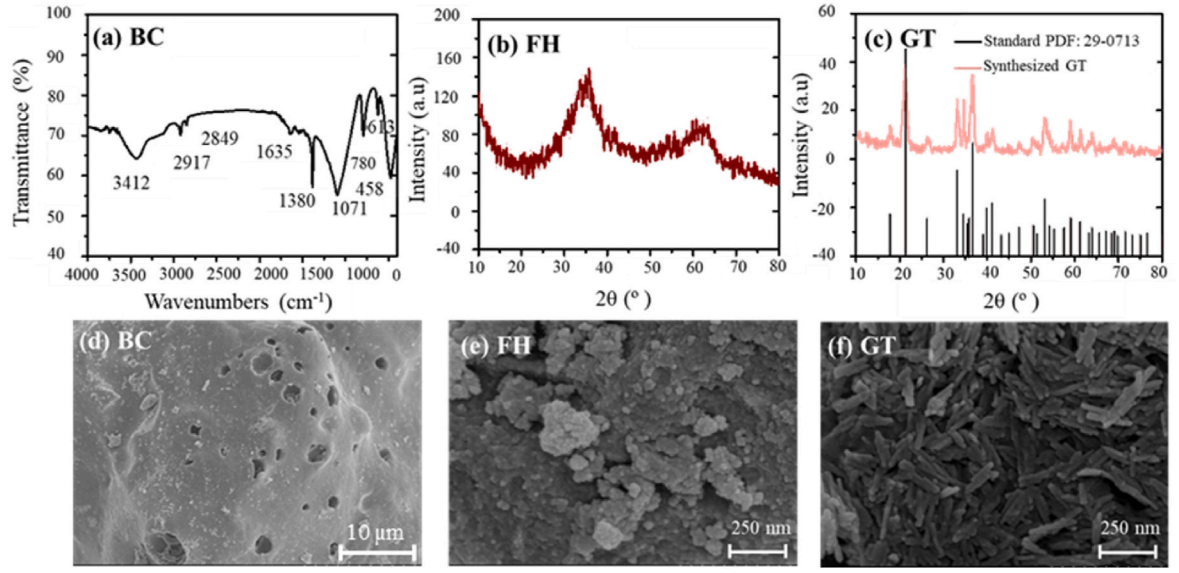

Fig. 1. FTIR spectrum of BC (a), XRD spectrum of FH (b), GT (c), and their SEM images (d–f).

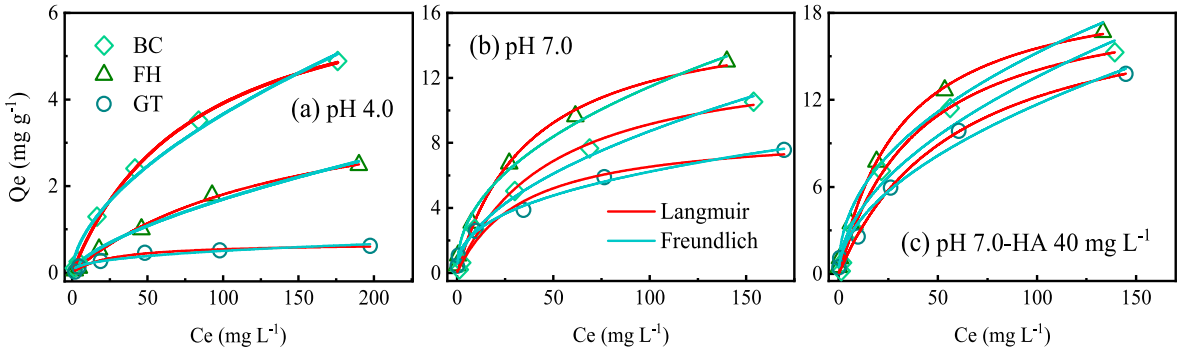

Fig. 2. Adsorption isotherms of Cd on BC, FH, and GT [pH 4.0 (a), pH 7.0 (b), and pH 7.0 with 40 mg L^{-1} HA (c)].

2.4. Analytical techniques

The micromorphological characteristics were investigated using field-emission scanning electron microscopy (SEM, JSM-7200 F, FEI Company) coupled with energy-dispersive X-ray spectroscopy (EDS) mapping of images obtained on a microscope operated at 25 kV. X-ray photoelectron spectroscopy (XPS, Escalab 250Xi, Thermo Scientific) and Fourier-transform infrared (FTIR, Vertex V80, Bruker) spectroscopy were used to characterize the surface functional groups, composition, and combination states of the elements after adsorption. In this study, an automatic mercury porosimeter (AutoPore 9500, Micromeritics) with two low-pressure stations and one high-pressure station was used to examine the porosity.

3. Results and discussion

3.1. Characterization of biochar and iron oxides

The pH values for BC, GT, and FH were 10.1, 8.6, and 7.9, respectively, and their specific surface areas were 2.1 $m^2 g^{-1}$, 89.0 $m^2 g^{-1}$, and 203.6 $m^2 g^{-1}$, respectively. The FTIR spectrum of BC showed apparent adsorption peaks at 3412, 1635, 1380, 1070, and 780 cm^{-1} (Fig. 1), which were assigned to the –OH, –C═O, –C–H, –C–O, and –CH═CH– groups, respectively (Ngambia et al., 2019). The synthesized FH and GT were pure and contained no other impurities; this was confirmed by XRD and SEM (Fig. 1) as described in our previous study (Chen et al., 2019; Ma et al., 2018). The synthesized FH was two-line and amorphous, and the micromorphology showed an ellipsoidal shape (Fig. 1e). The GT micromorphology was needle-shaped (Fig. 1f, approximately 10 and 100 nm in width and length, respectively) and had a crystal structure, which was matched with a standard PDF card (Fig. 1c, black line). In a neutral solution, both FH and GT particles agglomerated to form larger particles. The SEM images of BC (Fig. 1d), revealed abundant pores and different pore sizes (from the mesopore level to the micrometer level) on the rough surface of BC.

3.2. Cd adsorption onto biochar and iron oxides

The adsorption isotherms of Cd onto BC, FH, and GT are shown in Fig. 2 and the Langmuir and Freundlich adsorption model results are shown in Table S1. The Cd adsorption onto all adsorbents at pH 7.0 was higher than that at pH 4.0, which is consistent with the results of Zhou et al. (2018). At pH 4.0, the order of the Cd adsorption capacity was: BC (7.09 mg g^{-1}) > FH (4.35 mg g^{-1}) > GT (0.68 mg g^{-1}) (Table S1). Under the same pH conditions, the Cd adsorption of BC was markedly greater than that of GT (Zhu et al., 2020). We inferred that the larger number of pores in BC is an important reason for its stronger adsorption capacity compared to that of iron oxides. Previous studies have demonstrated that heavy metals adsorption onto BC can be improved by optimizing its pore distribution and surface area (Jin et al., 2014). The high surface area and pore volume enhance the transfer of Cd to the pores of BC and provide additional opportunities for metal active sites to bind Cd ion

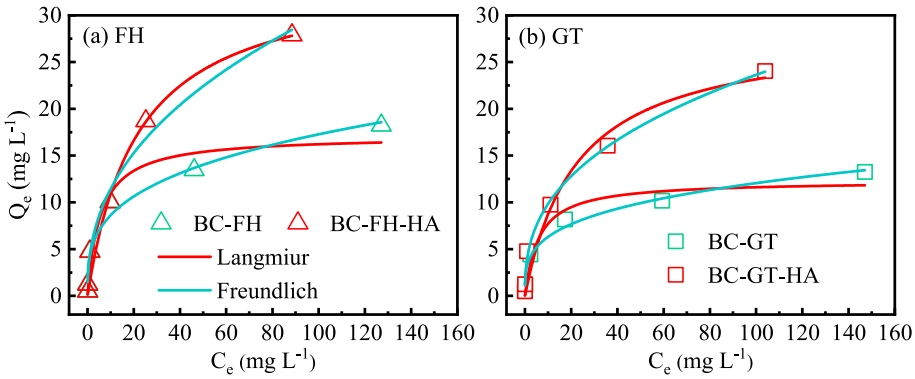

Fig. 3. Adsorption isotherms of Cd on BC-FH (a) and BC-GT (b) under the influence of HA (pH = 7.0).

(Trakal et al., 2014). Because the specific surface area of FH was larger than that of BC, the Cd adsorption capacity of FH was greater than that of BC and GT.

The Langmuir model ($R^2 > 0.987$) had superior fitted results compared to the Freundlich model ($R^2 > 0.942$) (Fig. 2), which indicates that the Cd adsorption on these adsorbents tends to be of the monolayer type. HA increased the adsorption for Cd, and the adsorption capacity of FH was the highest (20.4 mg g^{-1}), followed by BC (19.7 mg g^{-1}), and that of GT was the lowest (19.5 mg g^{-1}) (Fig. 2 and Table S1). The presence of HA enhanced the Cd adsorption capacities of these adsorbents by 26.1, 44.2, and 122.0%, respectively, compared to those in the absence of HA. Moreover, after the addition of HA, the difference in the Cd adsorption capacities of BC, FH, and GT was reduced significantly, thereby indicating that HA strongly influences the adsorption of Cd. Park et al. (2017) reported that the presence of HA enhanced the absorption of Cd by BC at low pH. This was attributed to the HA-coated BC having more negatively charged surfaces, and less aggregation of BC particles increased its adsorption sites.

3.3. Cd adsorption onto biochar-iron oxide complexes

The adsorption isotherms of BC-iron oxide complexes on Cd are shown in Fig. 3, and the relevant fitting parameters are shown in Table S2. Compared to the Langmuir model, the Freundlich model was more suitable for describing the adsorption isotherms. To clarify the synergistic effect between iron oxides and BC, we used the average value of the equilibrium adsorption capacity of BC and FH for Cd, as the addition ratio in the composite system was 1:1. The Cd adsorption of BC-FH (17.1 mg g^{-1}) was higher than the average adsorption of BC and FH (14.9 mg g^{-1}), and the efficiency was enhanced by 15.0%. Similarly, the

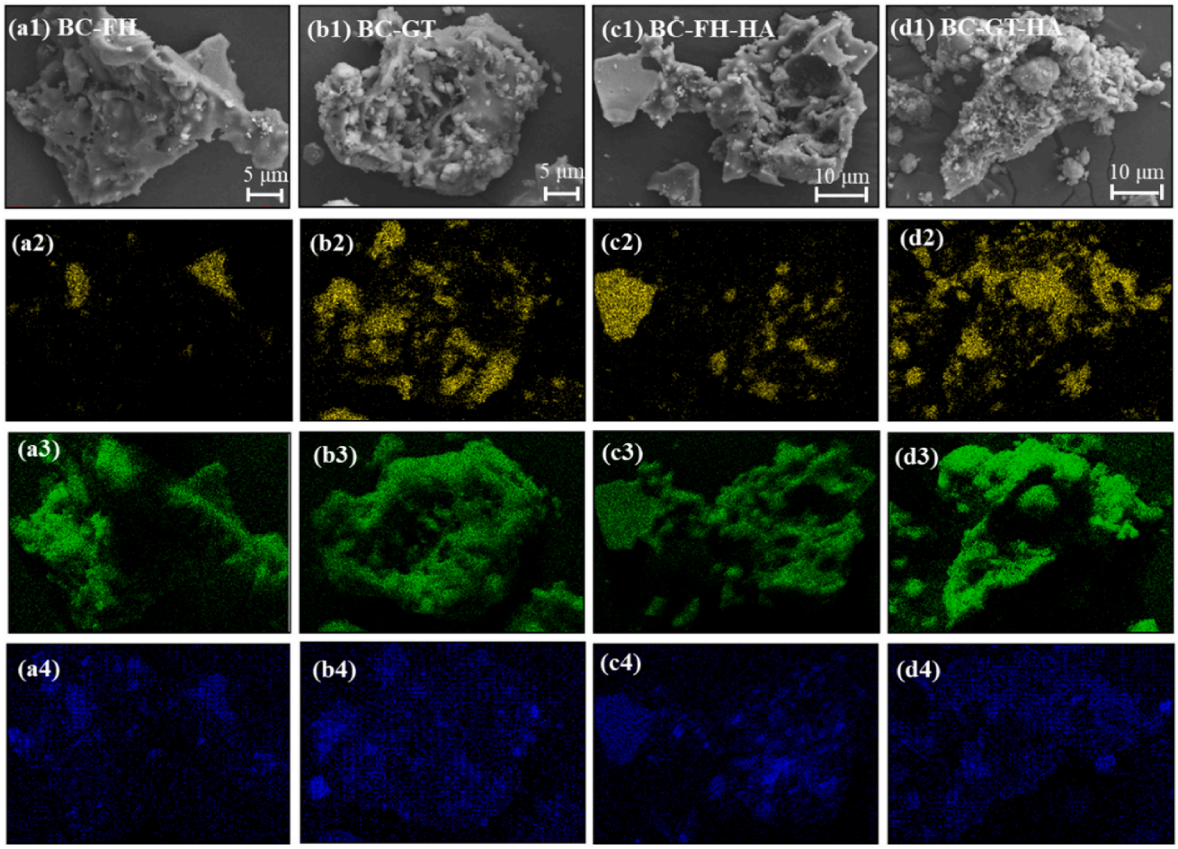

Fig. 4. Morphology and elemental mapping (yellow, Fe; green, O; and blue, Cd) of BC-FH (a), BC-GT (b), BC-FH-HA (c), and BC-GT-HA (d). (For interpretation of the references to color in this figure legend, the reader is referred to the Web version of this article.)

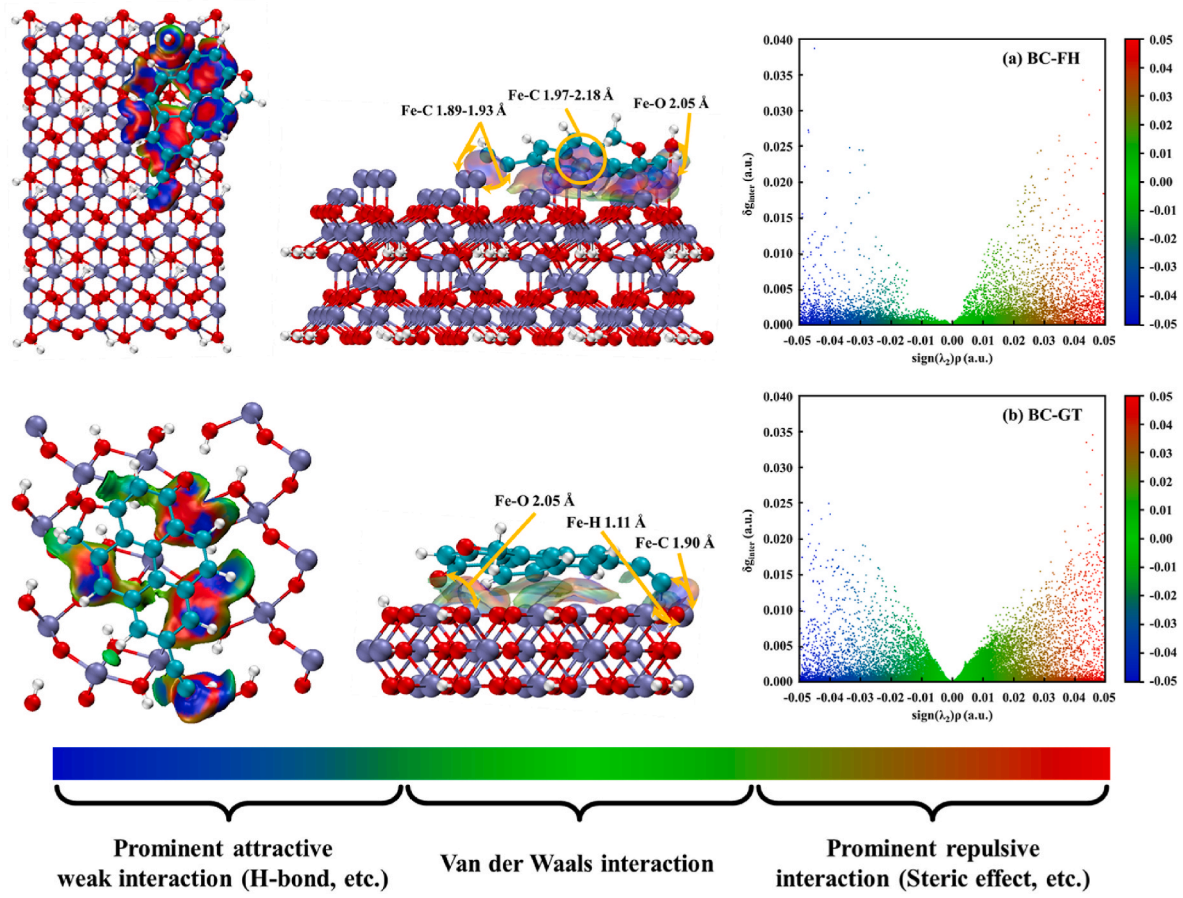

Fig. 5. Visualization of weak interaction regions of the independent gradient model (IGM) with different perspectives and isovalues of 0.01 a. u. and the corresponding scatter maps. Cluster model of the structures of BC and representative iron oxides: BC-FH (a) and BC-GT (b). H, C, O, and Fe are labeled by white, cyan, red, and bluish violet, respectively. (For interpretation of the references to color in this figure legend, the reader is referred to the Web version of this article.)

adsorption capacity of BC-GT (12.3 mg g^{-1}) was higher than that of BC and GT (11.1 mg g^{-1}), and the corresponding increase in efficiency was 10.8% (Fig. 3 and Table S2). In other studies, compared to single adsorption, the combined adsorption of heavy metals significantly increased the oxide binding state, and the adsorption capacity of Cd increased by 30% (Liu et al., 2020). This may have resulted from the tight binding in BC-FH and BC-GT, and the synergistic effect of BC and iron minerals may have improved the oxidation capacity of the materials; thus, more Cd could have been adsorbed and combined to form an oxide binding state (Wang et al., 2019). These results indicate that there was a synergistic effect between BC and iron oxides (Yang et al., 2018).

Humic acid also increased the adsorption of Cd by the BC-iron oxide complex, and its effect on BC-FH was more significant. In the presence of HA, the Cd adsorption isotherms were also closely fitted by the Freundlich isothermal adsorption model ($R^2 > 0.99$), showing that the mechanism of Cd adsorption did not change after HA loading. We believe that the improvement in the adsorption of the composites was based on the interaction and bonding modes of the two materials.

3.4. Interaction of biochar-iron oxide complexes

3.4.1. Morphology of biochar-iron oxide complexes

According to the SEM-EDS mapping images, both FH and GT combined and interacted with BC (Fig. 4a and b). The FH particles entered the pores of the BC, and only some were adsorbed on the surface (Fig. 4a1). Correspondingly, most GT particles were restrained on the surface of BC (Fig. 4b1), owing to the elongated form of GT. HA ensured the dispersion of FH, whereas it increased the agglomeration of GT resulting in the formation of larger particles (Chen et al., 2019), thus preventing GT from entering the pores of BC and further increasing its loading on the surface of BC. As shown in Fig. 4 and S1, in the presence of HA, the FH particles were smaller than those of GT (Ma et al., 2020), which allowed more FH to enter the pores and increase the loading inside the BC pores than that by GT.

3.4.2. Quantum chemical analysis

To further elucidate the interactions between BC and iron oxides, quantum chemical computations were performed. Based on the promolecular electron density, IGM can be used to investigate interfragments (δg^{inter}) and vividly present weak interaction regions (Lefebvre et al., 2017; Rayene et al., 2022; Wu et al., 2022b). In this study, δg^{inter} was used to clarify the interaction regions between BC and the two types of iron oxides. The prominent repulsive interaction, van der Waals interaction (I_{VDW}), and strongly attractive interaction (H-bond) surfaces can be distinguished by colors [blue–green–red (BGR)]. In the colored scatter maps, every point was matched with a grid point in the 3D space (Lefebvre et al., 2017; Lu and Chen, 2022). In the BC-FH system, the BC is almost parallel to the FH (Fig. 5a), result in a large area of interaction between BC and FH, further producing a strong I_{VDW} (Liu et al., 2022). The distance of C atoms in the BC molecule between Fe atoms in FH was short (1.89–2.18 Å) and caused a covalent-like bond interaction. The hydroxyl group on the benzene ring in the BC molecule tended to transfer to FH. According to the scatter maps, a larger I_{VDW} angle between the BC molecule and GT was observed in the BC-GT system (Fig. 5). Interatomic interactions existed in Fe–O (2.05 Å), Fe–H (1.11 Å), and Fe–C (1.90 Å) (Fig. 5b). Although an obvious peak did not appear around sign $(\lambda_2)\rho = -0.02$ to -0.05 (Fig. 5), the C–H group of benzene formed a very weak H-bond with the O atom of oxygen-bearing

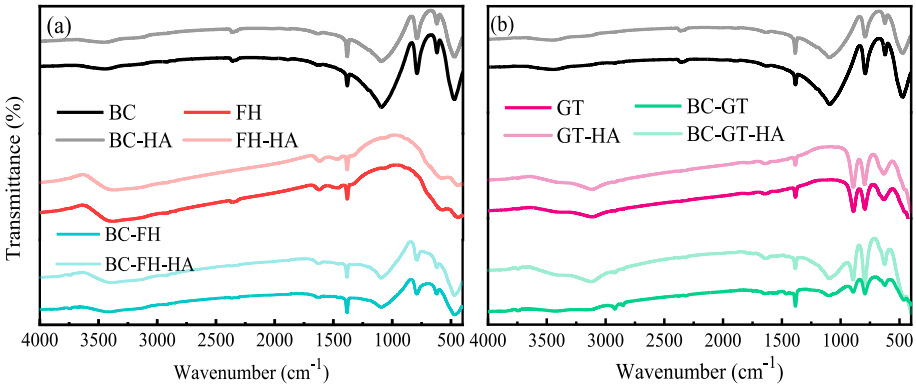

Fig. 6. FTIR spectra of BC, iron oxides (FH and GT), and their complexes.

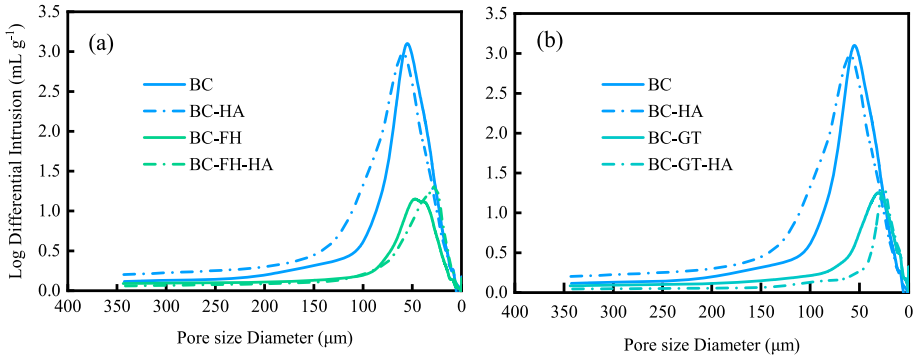

Fig. 7. Pore structure analysis of BC and iron oxides (FH (a) and GT (b)) and their complexes influenced by HA.

minerals (Dawley et al., 2012; Wu et al., 2022a). Moreover, the close atomic distances indicated that covalent-like interactions were likely to form between atoms. We believe that the I_{VDW}, H-bonds, and covalent-like interactions maintain a stable combination of iron minerals and BC.

3.4.3. *Effect of functional groups on interactions between biochar and iron oxides*

The surface oxygen-containing functional groups strongly influenced the interactions between the surface functional groups of BC and iron oxides. Quantum chemical calculations only reflected the interaction between characteristic functional groups on BC and iron minerals, and the FTIR results made the analysis comprehensive. FTIR spectra of BC and iron oxides showed that the absorption band in the high wavenumber region was caused by –OH stretching (3423–3444 cm^{-1}) (Wang et al., 2022) and at lower wavenumbers as a result of Fe–O lattice vibration (approximately 887 cm^{-1}) (Liang et al., 2020). These bands have been previously reported for pure iron oxides (Chen et al., 2011). The surface of BC exhibits weak –OH stretching and strong –C–O (1071 cm^{-1}), –C–OH (1071 cm^{-1}), –C═O (1600 cm^{-1}), and –CH═CH– (780 cm^{-1}) stretching (Chen et al., 2008). After the iron oxide loaded onto surface, the number of carboxyl and hydroxyl groups increased (Fig. 6). The –OH and –C═O stretching were strengthened, whereas the absorption peaks of the –C–O, C–OH, and –CH═CH– were shifted to lower frequencies, indicating that these functional groups may be complexed with iron oxides. During the loading process, the absorption peak intensity of these functional groups on the surface of BC-GT decreased more than that on BC-FH (Fig. 6). This could be attributed to GT being more likely to form suspended nanoparticles as well as the presence of a large mass of GT nanoparticles on the BC surface. This is consistent with the SEM-EDS results (Fig. 4b2). In the presence of HA, the FTIR spectrum of the BC-iron oxide complex was similar to that of iron oxides, indicating that HA mainly binds to iron oxides.

3.4.4. *Pore structure analysis*

The pore size as a function of log differential intrusion is shown in Fig. 7, and the pore size distributions of BC and iron oxide are listed in Table S3. The porosity and average pore diameter of the BC were 71.7% and 234.2 nm, respectively. The porosity and average pore diameter of BC after FH loading were reduced to 62.4% and 175.6 nm, respectively, and after GT loading, they were 67.6%, and 133.8 nm, respectively. Similarly, the specific surface area, total pore volume, and total pore area of BC were also reduced after FH and GT were loaded. The porosity of BC decreased significantly with FH loading (9.3%) compared to GT loading (4.1%) (Fig. 4). This is consistent with the SEM-EDS results. The reduction in these parameters indicates that iron oxides entered and blocked some of the pores of BC, and that the plugging effect of FH on BC pores was greater than that of GT. According to the above quantum chemical calculations (Fig. 5), we believe that the strong I_{VDW} generated by the almost parallel crystal structure between BC-FH molecules is an important factor that leads to a higher BC pore clogging rate than that of GT. Moreover, the porosity, average pore diameter, total pore volume, and total pore area of BC increased after HA loading. We inferred that this was caused by impurities such as salt and fine carbon particles, in the macropores of BC being successfully “cleaned” through complexation or ligand exchange after the addition of HA (Gong et al., 2020; Niu et al., 2021). Compared with the BC-iron oxide complex, the pore size distribution characteristics were further reduced when HA was present, which was caused by the agglomerate formation that further blocked the pore structure of BC. As shown in Fig. 7, the peak of the pore size distribution curves shifted to the left (small pore size) after the addition of HA. These results further proved that the agglomerates of BC-iron oxides were formed, and that the agglomerates preferentially blocked the macropore size of BC.

In brief, FH and GT combined and interacted with BC. Most of the FH particles entered the pores of BC and thus blocked them, whereas GT particles were mostly loaded on the surface of BC owing to their larger

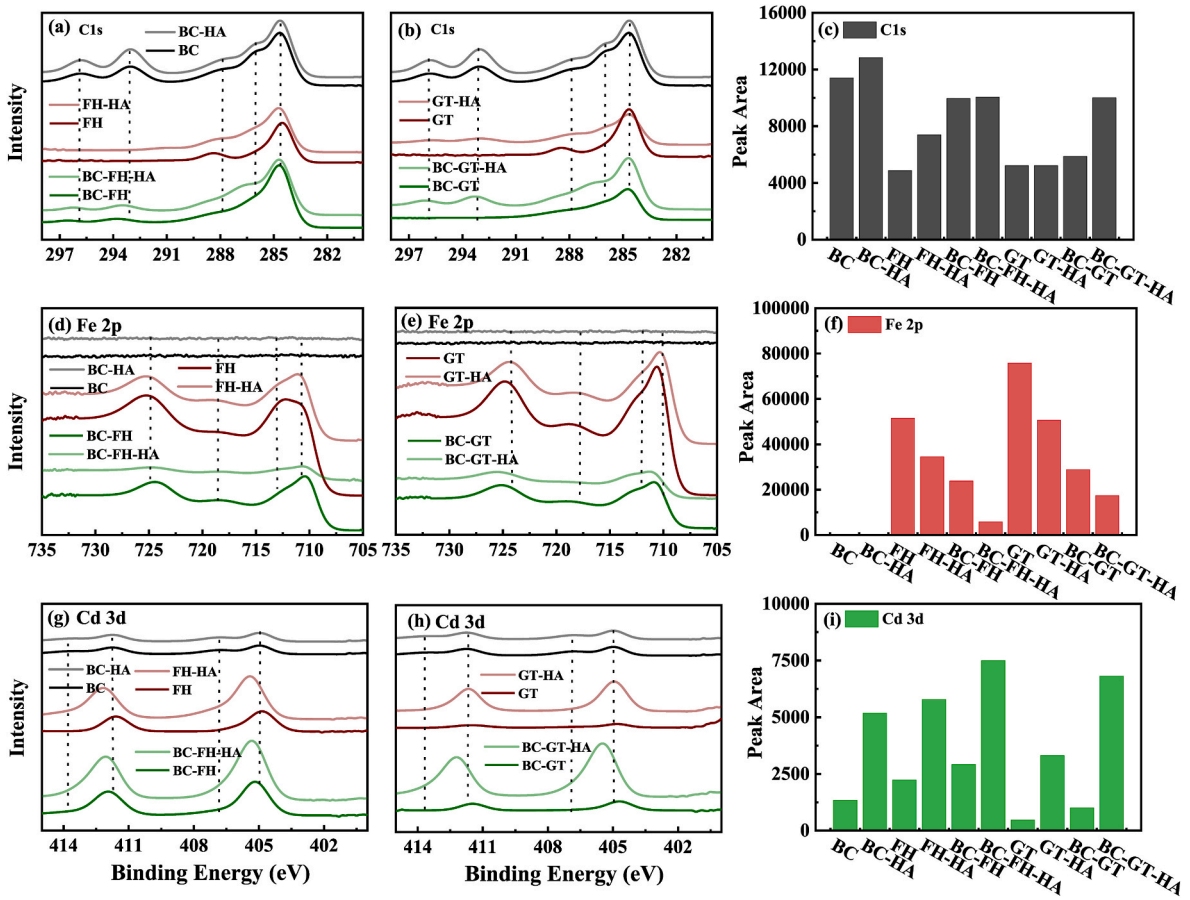

Fig. 8. XPS high resolution spectra of BC, iron oxides (FH and GT), and their complexes (BC-FH and BC-GT) on C 1s (a–c), Fe 2p (d–f), and Cd 3 d (g–i) adsorption rates and the effect of HA, respectively (pH = 7.0).

morphology. The quantum chemical calculations and infrared analysis fully reflect the interactions between the characteristic functional groups and iron minerals on BC as well as the influence of the interactions between functional groups. The interactions of I_{VDW}, H-bonds, and covalent-like interactions maintained a stable combination between BC and iron minerals. Moreover, HA ensured the dispersion of FH, whereas it increased agglomeration of GT. Stable interactions and stereoscopic pore filling occurred between BC and FH.

3.5. Cd binding on biochar-iron oxides

3.5.1. XPS analysis of adsorbed Cd on biochar-iron oxide complexes

To further explore the removal mechanism of Cd, high-resolution XPS of C 1s, Fe 2p, and Cd 3 d was performed on BC, FH, GT, and their complexes before and after HA loading (Fig. 8 and S2). Peaks of C 1s high-resolution spectra appearing at binding energies of 288.5, 286.1, and 284.8 eV were characteristic peaks of O–C═O, C–O, and C–C, respectively (Singh et al., 2014). The total C 1s photoelectron spectral intensity weakened as FH and GT were bound on the surface of BC, and the C–O and O–C═O peaks were reduced significantly. This confirmed that chemical interactions occurred between BC and iron oxides. Based on the obtained C 1s envelope, after FH and GT were loaded onto BC, the relative content of C–O increased by 44.7% and 27.6%, respectively, and the content of O–C═O decreased by 28.5% and 14.4% (Fig. 8 and S2), respectively. The results showed that iron oxides mainly interacted with the carboxyl groups of BC. This was consistent with previous quantum chemical analysis results. These changes also occurred after HA loading, and the effect of HA on FH was more pronounced than that on GT.

The XPS spectrum of BC did not show an Fe photoelectron signal, whereas FH and GT had strong Fe 2p photoelectron signals. The Fe 2p spectrum showed two peaks of Fe 2p3/2 and 2p1/2 at binding energy positions of ~712.2 and ~725.8 eV (Cui et al., 2021), respectively, for bulk FH and GT. The observed binding energy difference between 2p3/2 and 2p1/2 was ~13.6, which was confirmed by the iron oxide phase; more specifically, the Fe_2O_3, FeOOH, and Fe^{3+} were released by them (Wang et al., 2017). After HA loading, there was a significant shift in the position of the peak maxima in the Fe 2p doublet; the binding energy positions were approximately 710.5 eV (for Fe 2p3/2) and 724.1 eV (for Fe 2p1/2) (Fig. 8 and S2). The low-binding-energy side of the envelope accounted for the formation of the lower oxidation state Fe^{2+} ions (Yuan et al., 2020). This finding indicates a reduction of Fe^{3+} to Fe^{2+}. The same trend was observed when BC was present; the photoelectron spectral intensity weakened, and the maximum peak was shifted to a low binding energy position. These oxygen-containing functional groups on the surface would enhance complexation of Cd.

The adsorbed Cd exhibited varying forms on the adsorbents following its adsorption at pH 7.0, and mainly Cd^{2+} (405.7 eV and 411.7 eV), Cd $(OH)_2$ (406.7 eV), and CdO (412.8 eV) forms were adsorbed (Fig. 8 and S2). The adsorbed Cd on the surface of the iron oxides and the BC-iron oxide complex was mainly Cd^{2+}, which coordinated with oxygen-containing functional groups (Cui et al., 2021). The elemental distribution of adsorbed Cd with the Fe distribution was less than that of the area with the O distribution (Fig. 4b, c and d), indicating that Cd bonds to O, regardless of its adsorption by BC or iron minerals. We inferred that the combination of the BC and iron minerals formed a more complex interwoven structure of oxygen-containing functional groups (Xie et al., 2020), which enhanced the Cd adsorption. The pore filling of FH extended the intricate relationship of functional groups into the pores. Therefore, BC-FH displayed a stronger adsorption capacity for Cd than that of BC-GT. In the presence of HA, the photoelectron peaks of

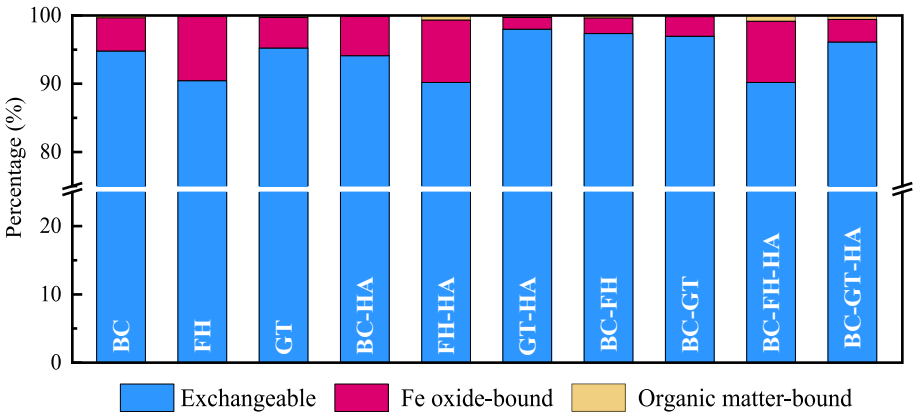

Fig. 9. Combined morphology of BC, iron oxides (FH and GT), and their complexes (BC-FH and BC-GT) adsorbing Cd under the influence of HA.

Cd 3 d increased in BC, FH, GT, and their complexes, which indicated an increased adsorption capacity of Cd which was possibly achieved through modifying the functional groups (e.g., COOH and/or OH) on the surface of these adsorbents, intensifying the negative charges on their surfaces, and increasing the Cd adsorption through complexation and electrostatic attraction (Zhou et al., 2018). The order of the Cd 3 d peak area for the bulk materials was FH > BC > GT, and that for the complex was BC-FH > BC-GT. These results are consistent with those of the Cd adsorption isotherms. Humic acid promoted the dispersion of FH, whereas it enhanced the agglomeration of GT, thus HA was more effective in enhancing the Cd adsorption by BC-FH. Moreover, the highly aromatic component of HA was strongly hydrophobic, which caused the hydrophilic Cd to be enriched.

3.5.2. *Adsorbed Cd fractions*

The BCR results showed that the binding forms of Cd on BC and iron oxides mainly existed in the water/acid-soluble and exchangeable fraction (F1), with a relative proportion of more than 92% (Fig. 9). This corresponds to the existence of Cd in the ion adsorption state of the +2 valency in the XPS analysis. The exchangeable fraction was the most labile in the environmental samples and was therefore the most bioavailable and hazardous for the environment. The exchangeable fraction (F1) of GT was significantly higher than that of FH under all conditions except when iron minerals were bound to BC. A reducible fraction (F2, approximately 8%) represented Cd bound to Fe oxyhydroxide (Fig. 9). Fraction 3 was mainly composed of Cd bound to organic compounds, and the proportion of this component is minimal and can be ignored (Fig. 9). In the presence of HA, the proportion of Fraction 3 slightly increased, which may have resulted from the enhanced adsorption of Cd by HA through electrostatic attraction and complexation (Zhao et al., 2022); this is consistent with the analysis above. However, the most unstable fraction (F1) always had high proportions (approximate 90%), thereby indicating that these materials cannot strongly fix Cd. The risk of Cd release into the environment was high.

4. Conclusion

This study revealed that the synergistic effect between BC and iron oxides increases the Cd adsorption. The Cd adsorption efficiencies of BC-GT and BC-FH were increased by 10.8% and 15%, respectively. The Cd adsorption capacity and enhanced adsorption efficiency of BC-FH were more pronounced than those of BC-GT because BC was more tightly bound to FH than to GT. Both FH and GT mainly interacted with the carboxyl groups of BC, and I_{VDW}, H-bonds, and covalent-like interactions maintained a stable combination between BC and iron minerals. Most FH particles entered the pores of BC, whereas GT particles were restrained on the surface of BC, especially in the presence of HA. Stable interactions and stereoscopic pore filling led to a stronger adsorption capacity of BC-FH for Cd. Moreover, the binding forms of Cd adsorbed by BC, iron minerals, and composite materials were mainly exchangeable, whereas the proportion of the oxide-binding state and organic matter-binding state was relatively low, the adsorption was not strong, and the adsorbed Cd was easily released into the environment, increasing the risk of environmental pollution. The effects of various ions in soil pore environment on Cd adsorption by composite materials need to be further studied.

Authors contributions

Yong Liu: Formal analysis, writing—original draft and writing—review & editing. Long Wang: Formal analysis, writing—original draft and writing—review & editing. Chang Liu: Investigation. Jie Ma: Formal analysis, writing—original draft, writing—review & editing, Methodology, and visualization. Xiaoxue Ouyang: writing—original draft. Liping Weng: Supervision and project administration. Yali Chen: Project administration. Yongtao Li: Funding acquisition.

Funding

The study is financially supported by the National Natural Science Foundation of China (No. 41701262 and 42007103), Key Projects at the Institute of Innovation Engineering, and The Science and Technology Fund of Henan Agricultural University (KJCX 2020A18).

Declaration of competing interest

The authors declare that they have no known competing financial interests or personal relationships that could have appeared to influence the work reported in this paper.

Data availability

Data will be made available on request.

Appendix A. Supplementary data

Supplementary data to this article can be found online at https://doi.org/10.1016/j.jenvman.2022.117136.

References

Ahmad, M., Rajapaksha, A.U., Lim, J.E., Zhang, M., Bolan, N., Mohan, D., Vithanage, M., Lee, S.S., Ok, Y.S., 2014. Biochar as a sorbent for contaminant management in soil and water: a review. Chemosphere 99, 19–33.

Ahmad, Z., Gao, B., Mosa, A., Yu, H.W., Yin, X.Q., Bashir, A., Ghoveisi, H., Wang, S.S., 2018. Removal of Cu(II), Cd(II) and Pb(II) ions from aqueous solutions by biochars derived from potassium-rich biomass. J. Clean. Prod. 180, 437–449.
Ali, J., Wang, H.B., Ifthikar, J., Khan, A., Wang, T., Zhan, K., Shahzad, A., Chen, Z.L., Chen, Z.Q., 2018. Efficient, stable and selective adsorption of heavy metals by thio-functionalized layered double hydroxide in diverse types of water. Chem. Eng. J. (Lausanne) 332, 387–397.
Amini, M., Antelo, J., Fiol, S., Rahnemaie, R., 2020. Modeling the effects of humic acid and anoxic condition on phosphate adsorption onto goethite. Chemosphere 253, 126691.
Chappell, H.F., Thom, W., Bowron, D.T., Faria, N., Hasnip, P.J., Powell, J.J., 2017. Structure of naturally hydrated ferrihydrite revealed through neutron diffraction and first-principles modeling. Phy Rev Mater 1.
Chen, B., Chen, Z., Lv, S., 2011. A novel magnetic biochar efficiently sorbs organic pollutants and phosphate. Bioresour. Technol. 102, 716–723.
Chen, B., Zhou, D., Zhu, L., 2008. Transitional adsorption and partition of nonpolar and polar aromatic contaminants by biochars of pine needles with different pyrolytic temperatures. Environ. Sci. Technol. 42, 5137–5143.
Chen, Y., Ma, J., Li, Y., Weng, L., 2019. Enhanced cadmium immobilization in saturated media by gradual stabilization of goethite in the presence of humic acid with increasing pH. Sci. Total Environ. 648, 358–366.
Cui, L., Li, L., Bian, R., Ippolito, J.A., Yan, J., Quan, G., 2021. Physicochemical disintegration of biochar: a potentially important process for long-term cadmium and lead sorption. Biochar 3, 511–518.
Cui, X., Fang, S., Yao, Y., Li, T., Ni, Q., Yang, X., He, Z., 2016. Potential mechanisms of cadmium removal from aqueous solution by Canna indica derived biochar. Sci. Total Environ. 562, 517–525.
Dai, S., Wang, B., Song, Y., Xie, Z., Li, C., Li, S., Huang, Y., Jiang, M., 2021. Astaxanthin and its gold nanoparticles mitigate cadmium toxicity in rice by inhibiting cadmium translocation and uptake. Sci. Total Environ. 786, 147496.
Dawley, M.M., Scott, A.M., Hill, F.C., Leszczynski, J., Orlando, T.M., 2012. Adsorption of formamide on kaolinite surfaces: a combined infrared experimental and theoretical study. J. Phys. Chem. C 116, 23981–23991.
Frisch, M.J., Trucks, G.W., Schlegel, H.B., Scuseria, G.E., Robb, M.A., Cheeseman, J.R., Scalmani, G., Barone, V., Petersson, G.A., Nakatsuji, H., Li, X., Caricato, M., Marenich, A.V., Bloino, J., Janesko, B.G., Gomperts, R., Mennucci, B., Hratchian, H. P., Ortiz, J.V., Izmaylov, A.F., Sonnenberg, J.L., Williams-Young, D., Ding, F., Lipparini, F., Egidi, F., Goings, J., Peng, B., Petrone, A., Henderson, T., Ranasinghe, D., Zakrzewski, V.G., Gao, J., Rega, N., Zheng, G., Liang, W., Hada, M., Ehara, M., Toyota, K., Fukuda, R., Hasegawa, J., Ishida, M., Nakajima, T., Honda, Y., Kitao, O., Nakai, H., Vreven, T., Throssell Jr., K., Montgomery, J.A., Peralta, J.E., Ogliaro, F., Bearpark, M.J., Heyd, J.J., Brothers, E.N., Kudin, K.N., Staroverov, V.N., A, K.T., Kobayashi, R., Normand, J., Raghavachari, K., Rendell, A.P., Burant, J.C., Iyengar, S.S., Tomasi, J., Cossi, M., Millam, J.M., Klene, M., Adamo, C., Cammi, R., Ochterski, J.W., Martin, R.L., Morokuma, K., Farkas, O., Foresman, J.B., Fox, D.J., 2016. Gaussian 16, Revision B.01. Gaussian, Inc., Wallingford CT.
Fu, H., Ma, S., Xu, S., Duan, R., Cheng, G., Zhao, P., 2021. Hierarchically porous magnetic biochar as an efficient amendment for cadmium in water and soil: performance and mechanism. Chemosphere 281.
Gong, X.J., Li, Y.S., Dong, Y.Q., Li, W.G., 2020. Arsenic adsorption by innovative iron/calcium in-situ-impregnated mesoporous activated carbons from low-temperature water and effects of the presence of humic acids. Chemosphere 250, 126275.
Goswami, R., Shim, J., Deka, S., Kumari, D., Kataki, R., Kumar, M., 2016. Characterization of cadmium removal from aqueous solution by biochar produced from Ipomoea fistulosa at different pyrolytic temperatures. Ecol. Eng. 97, 444–451.
Hussain, A., Rizwan, M., Ali, S., Rehman, M.Z.U., Qayyum, M.F., Nawaz, R., Ahmad, A., Asrar, M., Ahmad, S.R., Alsahli, A.A., Alyemeni, M.N., 2021. Combined use of different nanoparticles effectively decreased cadmium (Cd) concentration in grains of wheat grown in a field contaminated with Cd. Ecotoxicol. Environ. Saf. 215, 112139.
Jefferson, W.A., Hu, C., Liu, H., Qu, J., 2015. Reaction of aqueous Cu-Citrate with MnO2 birnessite: characterization of Mn dissolution, oxidation products and surface interactions. Chemosphere 119, 1–7.
Jin, H., Capareda, S., Chang, Z., Gao, J., Xu, Y., Zhang, J., 2014. Biochar pyrolytically produced from municipal solid wastes for aqueous As(V) removal: adsorption property and its improvement with KOH activation. Bioresour. Technol. 169, 622–629.
Jing, L.A., Rz, A., Lm, A., Hfab, C., Xlab, C., Scp, D., E, M., 2021. Adsorption of Phosphate and Cadmium on Iron (Oxyhydr)oxides: A Comparative Study on Ferrihydrite, Goethite, and Hematite Geoderma 383.
Jung, K.W., Lee, S.Y., Lee, Y.J., 2018. Hydrothermal synthesis of hierarchically structured birnessite-type MnO2/biochar composites for the adsorptive removal of Cu(II) from aqueous media. Bioresour. Technol. 260, 204–212.
Lefebvre, C., Rubez, G., Khartabil, H., Boisson, J.C., Contreras-Garcia, J., Henon, E., 2017. Accurately extracting the signature of intermolecular interactions present in the NCI plot of the reduced density gradient versus electron density. Phys. Chem. Chem. Phys. 19, 17928–17936.
Li, J., Zhao, W., Du, H., Guan, Y., Ma, M., Rennenberg, H., 2022. The symbiotic system of sulfate-reducing bacteria and clay-sized fraction of purplish soil strengthens cadmium fixation through iron-bearing minerals. Sci. Total Environ. 820, 153253.
Liang, L., Li, X., Lin, Z., Tian, C., Guo, Y., 2019. The removal of Cd by sulfidated nanoscale zero-valent iron: the structural, chemical bonding evolution and the reaction kinetics. Chem. Eng. J. 382, 122933.
Liang, M., Xu, S., Zhu, Y., Chen, X., Deng, Z., Yan, L., He, H., 2020. Preparation and characterization of Fe-Mn binary oxide/mulberry stem biochar composite adsorbent and adsorption of Cr(VI) from aqueous solution. Int. J. Environ. Res. Publ. Health 17, 676.
Liu, K., Li, F., Cui, J., Yang, S., Fang, L., 2020. Simultaneous removal of Cd(II) and As(III) by graphene-like biochar-supported zero-valent iron from irrigation waters under aerobic conditions: synergistic effects and mechanisms. J. Hazard Mater. 395, 122623.
Liu, X., Wang, Y., Wang, W., Huang, W., Yu, Z., Zhou, S., 2021. Protein-derived structures determines the redox capacity of humic acids formed during hyperthermophilic composting. Waste Manag. 126, 810–820.
Liu, Y., Ma, J., Gao, J., Chen, X., Ouyang, X., Weng, L., Li, H., Chen, Y., Li, Y., 2022. Stability and interaction of biochar and iron mineral nanoparticles: effect of pH, ionic strength, and dissolved organic matter. Biochar 4.
Lu, T., 2021. Molclus Program, Version 1.9.9.6. http://www.keinsci.com/research/molclus.html. accessed Sep-4.
Lu, T., Chen, F., 2012. Multiwfn: a multifunctional wavefunction analyzer. J. Comput. Chem. 33, 580–592.
Lu, T., Chen, Q., 2022. Independent gradient model based on Hirshfeld partition: a new method for visual study of interactions in chemical systems. J. Comput. Chem. 43, 539–555.
Ma, J., Guo, H., Lei, M., Li, Y., Weng, L., Chen, Y., Ma, Y., Deng, Y., Feng, X., Xiu, W., 2018. Enhanced transport of ferrihydrite colloid by chain-shaped humic acid colloid in saturated porous media. Sci. Total Environ. 621, 1581–1590.
Ma, J., Jing, Y., Gao, L., Chen, J., Wang, Z., Weng, L., Li, H., Chen, Y., Li, Y., 2020. Hetero-aggregation of goethite and ferrihydrite nanoparticles controlled by goethite nanoparticles with elongated morphology. Sci. Total Environ. 748, 141536.
Ma, J., Lei, M., Weng, L., Li, Y., Chen, Y., Islam, M.S., Zhao, J., Chen, T., 2019. Fractions and colloidal distribution of arsenic associated with iron oxide minerals in lead-zinc mine-contaminated soils: comparison of tailings and smelter pollution. Chemosphere 227, 614–623.
Ma, J., Qiu, Y., Zhao, J., Ouyang, X., Zhao, Y., Weng, L., Yasir, A.M., Chen, Y., Li, Y., 2022. Effect of agricultural organic inputs on nanoplastics transport in saturated goethite-coated porous media: particle size selectivity and role of dissolved organic matter. Environ. Sci. Technol. 56, 3524–3534.
Maatar, W., Boufi, S., 2015. Poly(methacylic acid-co-maleic acid) grafted nanofibrillated cellulose as a reusable novel heavy metal ions adsorbent. Carbohydr. Polym. 126, 199–207.
Machado, M.D., Santos, M.S., Gouveia, C., Soares, H.M., Soares, E.V., 2008. Removal of heavy metals using a brewer's yeast strain of Saccharomyces cerevisiae: the flocculation as a separation process. Bioresour. Technol. 99, 2107–2115.
Navarro, R.R., Wada, S., Tatsumi, K., 2003. Heavy metal flocculation by phosphonomethylated-polyethyleneimine and calcium ions. Separ. Sci. Technol. 38, 2327–2345.
Ngambia, A., Ifthikar, J., Shahib II, Jawad, A., Shahzad, A., Zhao, M., Wang, J., Chen, Z., Chen, Z., 2019. Adsorptive purification of heavy metal contaminated wastewater with sewage sludge derived carbon-supported Mg(II) composite. Sci. Total Environ. 691, 306–321.
Niu, H., Yang, H., Tong, L., 2021. Adsorption behaviors of Au(III) onto humic acid extracted from gold ore: adsorptive kinetics, isotherm and mechanism. Colloid. Surface. 630.
O'Laughlin, J., McElligott, K., 2009. Biochar for Environmental Management: Science and Technology Forest Policy and Economics 11, 535–536.
Ouyang, X., Ma, J., Li, P., Chen, Y., Weng, L., Li, Y., 2021. Comparison of the effects of large-grained and nano-sized biochar, ferrihydrite, and complexes thereof on Cd and as in a contaminated soil-plant system. Chemosphere 280, 130731.
Park, C.M., Han, J.H., Chu, K.H., Al-Hamadani, Y.A.J., Her, N., Heo, J.Y., Yoon, Y.M., 2017. Influence of solution pH, ionic strength, and humic acid on cadmium adsorption onto activated biochar: experiment and modeling. J. Ind. Eng. Chem. 48, 186–193.
Park, J.H., Wang, J.J., Kim, S.H., Kang, S.W., Jeong, C.Y., Jeon, J.R., Park, K.H., Cho, J. S., Delaune, R.D., Seo, D.C., 2019. Cadmium adsorption characteristics of biochars derived using various pine tree residues and pyrolysis temperatures. J. Colloid Interface Sci. 553, 298–307.
Qian, X., Ma, J., Weng, L., Chen, Y., Ren, Z., Li, Y., 2020. Influence of agricultural organic inputs and their aging on the transport of ferrihydrite nanoparticles: from enhancement to inhibition. Sci. Total Environ. 719, 137440.
Randall, S.R., Sherman, D.M., Ragnarsdottir, K.V., Collins, C.R., 1999. The Mechanism of Cadmium Surface Complexation on Iron Oxyhydroxide Minerals. GEOCHIM COSMOCHIM AC.
Rayene, K., Imane, D., Abdelaziz, B., Leila, N., Fatiha, M., Abdelkrim, G., Bouzid, G., Ismahan, L., Brahim, H., Rabah, O., 2022. Molecular modeling study of structures, Hirschfield surface, NBO, AIM, RDG, IGM and 1HNMR of thymoquinone/hydroxypropyl-β-cyclodextrin inclusion complex from QM calculations. J. Mol. Struct. 1249.
Regmi, P., Moscoso, J., Kumar, S., Cao, X., Mao, J., Schafran, G., 2012. Removal of copper and cadmium from aqueous solution using switchgrass biochar produced via hydrothermal carbonization process. J. Environ. Manag. 109, 61–69.
Russell, B., Payne, M., Ciacchi, L.C., 2009. Density functional theory study of Fe(II) adsorption and oxidation on goethite surfaces. Phys. Rev. B 79.
Schwertmann, U., Cornell, R.M., 2008. Iron Oxides in the Laboratory Preparation and Characterization.
Singh, B., Fang, Y.Y., Cowie, B.C.C., Thomsen, L., 2014. NEXAFS and XPS characterisation of carbon functional groups of fresh and aged biochars. Org. Geochem. 77, 1–10.
Suresh Kumar, K., Dahms, H.U., Won, E.J., Lee, J.S., Shin, K.H., 2015. Microalgae - a promising tool for heavy metal remediation. Ecotoxicol. Environ. Saf. 113, 329–352.

Tian, H., He, Z., Wang, J., Jiao, H., Hu, Z., Yang, Y., 2020. Density functional theory study on the mechanism of biochar gasification in CO_2 environment. Ind. Eng. Chem. Res. 59, 19972–19981.
Trakal, L., Šigut, R., Šillerová, H., Faturíková, D., Komárek, M., 2014. Copper removal from aqueous solution using biochar: effect of chemical activation. Arab. J. Chem. 7, 43–52.
Valdrighi, M.M., Pera, A., Agnolucci, M., Frassinetti, S., Lunardi, D., Vallini, G., 1996. Effects of compost-derived humic acids on vegetable biomass production and microbial growth within a plant (Cichorium intybus)-soil system: a comparative study. Agric. Ecosyst. Environ. 58, 133–144.
Venema, P., Hiemstra, T., van Riemsdijk, W.H., 1996. Multisite adsorption of cadmium on goethite. J. Colloid Interface Sci. 183, 515–527.
Wang, B., Shang, C., Xie, H., Sun, H., Zhang, Q., Xue, L., Tack, F.M.G., Hou, D., Feng, Y., Rinklebe, J., 2022. Unraveling natural aging-induced properties change of sludge-derived hydrochar and enhanced cadmium sorption site heterogeneity. Biochar 4.
Wang, P., Ding, F., Huang, Z., Fu, Z., Zhao, P., Men, S., 2021. Adsorption behavior and mechanism of Cd (II) by modified coal-based humin. Environ. Technol. Innovat. 23.
Wang, S., Gao, B., Li, Y., Creamer, A.E., He, F., 2017. Adsorptive removal of arsenate from aqueous solutions by biochar supported zero-valent iron nanocomposite: batch and continuous flow tests. J. Hazard Mater. 322, 172–181.
Wang, S., Zhao, M., Zhou, M., Li, Y.C., Wang, J., Gao, B., Sato, S., Feng, K., Yin, W., Igalavithana, A.D., Oleszczuk, P., Wang, X., Ok, Y.S., 2019. Biochar-supported nZVI (nZVI/BC) for contaminant removal from soil and water: a critical review. J. Hazard Mater. 373, 820–834.
Wu, J., Liu, J., Wu, P., Sun, L., Chen, M., Shang, Z., Ye, Q., Zhu, N., 2022a. The heteroaggregation and deposition behavior of nanoplastics on Al2O3 in aquatic environments. J. Hazard Mater. 435, 128964.
Wu, J., Ye, Q., Wu, P., Xu, S., Liu, Y., Ahmed, Z., Rehman, S., Zhu, N., 2022b. Heteroaggregation of nanoplastics with oppositely charged minerals in aquatic environment: experimental and theoretical calculation study. Chem. Eng. J. 428.
Xie, S., Wang, L., Xu, Y., Lin, D., Sun, Y., Zheng, S., 2020. Performance and mechanisms of immobilization remediation for Cd contaminated water and soil by hydroxy ferric combined acid-base modified sepiolite (HyFe/ABsep). Sci. Total Environ. 740, 140009.
Yang, D., Wang, L., Li, Z., Tang, X., He, M., Yang, S., Liu, X., Xu, J., 2020. Simultaneous adsorption of Cd(II)andAs(III)by a novel biochar-supported nanoscale zero-valent iron in aqueous systems. Sci. Total Environ. 708, 134823.
Yang, F., Zhang, S., Li, H., Li, S., Cheng, K., Li, J.-S., Tsang, D.C.W., 2018. Corn straw-derived biochar impregnated with α-FeOOH nanorods for highly effective copper removal. Chem. Eng. J. (Lausanne) 348, 191–201.
Yin, K., Wang, J., Zhai, S., Xu, X., Li, T., Sun, S., Xu, S., Zhang, X., Wang, C., Hao, Y., 2022. Adsorption mechanisms for cadmium from aqueous solutions by oxidant-modified biochar derived from Platanus orientalis Linn leaves. J. Hazard Mater. 428, 128261.
Yuan, S., Liu, X., Gao, P., Han, Y., 2020. A semi-industrial experiment of suspension magnetization roasting technology for separation of iron minerals from red mud. J. Hazard Mater. 394, 122579.
Zhao, P., Huang, Z., Ma, Q., Zhang, B., Wang, P., 2022. Artificial humic acid synthesized from food wastes: an efficient and recyclable adsorbent of Pb (II) and Cd (II) from aqueous solution. Environ. Technol. Innovat. 27.
Zhou, Q., Liao, B., Lin, L., Qiu, W., Song, Z., 2018. Adsorption of Cu(II) and Cd(II) from aqueous solutions by ferromanganese binary oxide-biochar composites. Sci. Total Environ. 615, 115–122.
Zhu, L., Tong, L., Zhao, N., Li, J., Lv, Y., 2019. Coupling interaction between porous biochar and nano zero valent iron/nano alpha-hydroxyl iron oxide improves the remediation efficiency of cadmium in aqueous solution. Chemosphere 219, 493–503.
Zhu, S., Zhao, J., Zhao, N., Yang, X., Chen, C., Shang, J., 2020. Goethite modified biochar as a multifunctional amendment for cationic Cd(II), anionic As(III), roxarsone, and phosphorus in soil and water. J. Clean. Prod. 247.